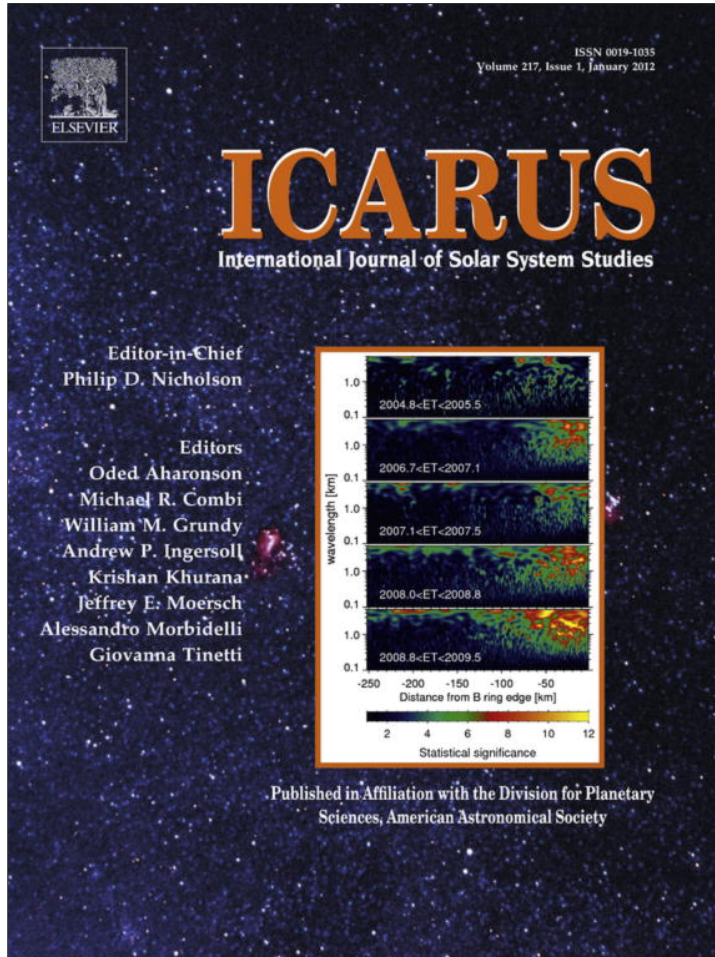


Provided for non-commercial research and education use.
Not for reproduction, distribution or commercial use.



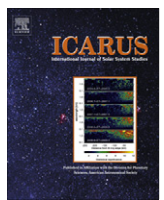
(This is a sample cover image for this issue. The actual cover is not yet available at this time.)

This article appeared in a journal published by Elsevier. The attached copy is furnished to the author for internal non-commercial research and education use, including for instruction at the authors institution and sharing with colleagues.

Other uses, including reproduction and distribution, or selling or licensing copies, or posting to personal, institutional or third party websites are prohibited.

In most cases authors are permitted to post their version of the article (e.g. in Word or Tex form) to their personal website or institutional repository. Authors requiring further information regarding Elsevier's archiving and manuscript policies are encouraged to visit:

<http://www.elsevier.com/copyright>



Impact-induced mantle dynamics on Mars

James H. Roberts ^{a,*}, Jafar Arkani-Hamed ^b

^aThe Johns Hopkins University Applied Physics Laboratory, 11100 Johns Hopkins Road, Laurel, MD 20723-6099, United States

^bDepartment of Physics, University of Toronto, 60 St. George St., Toronto, ON, Canada M5S 1A7

ARTICLE INFO

Article history:

Received 11 May 2011

Revised 18 October 2011

Accepted 30 November 2011

Available online 11 December 2011

Keywords:
Geophysics
Impact processes
Mars, interior
Thermal histories

ABSTRACT

At least 20 impact basins with diameters ranging from 1000 to 3380 km have been identified on Mars, with five exceeding 2500 km. The coincidental timing of the end of the sequence of impacts and the disappearance of the global magnetic field has led to investigations of impact heating crippling an early core dynamo. The rate of core cooling (and thus dynamo activity) is limited by that of the overlying mantle. Thus, the pre-existing thermal state of the mantle controls the extent to which a sequence of impacts may affect dynamo activity. Here, we examine the effects of the initial thermal structure of the core and mantle, and the location of an impact with respect to the pre-existing convective structure on the mantle dynamics and surface heat flux.

We find that the impacts that formed the five largest basins dominate the impact-driven effects on mantle dynamics. A single impact of this size can alter the entire flow field of the mantle. Such an impact promotes the formation of an upwelling beneath the impact site, resulting in long-lived single-plume convection. The interval between the largest impacts is shorter than the initial recovery time for a single impact. Hence, the change in convective pattern due to each impact sets up a long term change in the global heat flow. These long-term changes are cumulative, and multiple impacts have a synergistic effect.

© 2011 Elsevier Inc. All rights reserved.

1. Introduction

1.1. Observations

At least 20 exposed and buried “giant” impact basins with observed diameters, D_b exceeding 1000 km have been identified on Mars (Frey, 2008). Of these, five basins have $D_b > 2500$ km. The crater retention ages for these basins have been obtained by counting smaller craters, quasi-circular depressions (QCDs) in topography, and circular thin areas (CTAs) in crustal thickness models, with diameters greater than 300 km on the rims and interiors of the giant basins (Frey, 2008). The absolute model ages of these basins (Hartmann and Neukum, 2001) are largely clustered between 4.2 and 4.1 Ga. This spike in basin ages may be related to the Late Heavy Bombardment (Cohen et al., 2000; Gomes et al., 2005).

Observations of crustal magnetism (Acuña et al., 2001) provides strong evidence that such a global magnetic field existed early on, but vanished in the mid- to late Noachian. The ages of the basins correlate strongly with their magnetization strengths (Lillis et al., 2008), resulting in speculation that there may have been a causal relationship between the impacts which created the basins and the disappearance of the magnetic field (Arkani-Hamed et al., 2008; Roberts et al., 2009).

1.2. Previous work

The coincidental timing of the sequence of impacts and the disappearance of the magnetic field, suggests that former may have caused the latter (Arkani-Hamed et al., 2008; Roberts et al., 2009; Arkani-Hamed and Olson, 2010a,b). It is well known that large impacts can introduce substantial amounts of heating to planetary interiors (Reese et al., 2002; Monteux et al., 2007; Watters et al., 2009). Roberts et al. (2009) modeled the effects of impact heating on the mantle dynamics, in particular on the evolution of CMB heat flow. They found that the largest impacts heated the lower mantle resulting in a reduction in CMB heat flow that was unfavorable for a dynamo. Arkani-Hamed and Olson (2010a,b) on the other hand, suggested that direct impact heating of the core, with a lower specific heat than that of the mantle, may result in a substantial increase in core temperature and in the CMB heat flow. Moreover, the heating of the outer core results in stable stratification, which also serves to shut down dynamo activity. In both cases, a warm region, or “thermal blanket” prevents cooling of much of the core. In the first case, the thermal blanket is the lower mantle; in the second, it is the outermost core.

These previous studies have focused on the effects of basin-forming impacts in the deep interior and at the CMB. Here, we examine the effects of the initial thermal structure of the core and mantle, and the location of an impact with respect to the pre-existing convective structure on the mantle dynamics and surface heat flux.

* Corresponding author. Fax: +1 240 228 8939.

E-mail address: James.Roberts@jhuapl.edu (J.H. Roberts).

Table 1
Parameters for Noachian Mars.

Parameter	Symbol	Value	Reference
Planetary radius	R_0	3390 km	Bills and Ferrari (1978)
Core radius	R_c	1700 km	Yoder et al. (2003)
Mantle density	ρ_0	3500 kg m ⁻³	Sohl and Spohn (1997)
Gravitational acceleration	g	3.7 m s ⁻²	Esposito et al. (1992)
Coefficient of thermal expansion (at surface)	α_0	3×10^{-5} K ⁻¹	Roberts and Zhong (2004)
Coefficient of thermal diffusion (at surface)	κ_0	1.29×10^{-6} m ² s ⁻¹	Schatz and Simmons (1972)
Specific heat	C_p	1200 J kg ⁻¹ K ⁻¹	Roberts and Zhong (2004)
Surface temperature	T_0	220 K	Roberts and Zhong (2004)
Initial CMB temperature	T_{CMB}	2000 K	Nimmo and Stevenson (2000) and Hauck and Phillips (2001)

Table 2
Radioactive heating parameters for bulk silicate Mars.

Isotope	Present-day concentration	Half-life (Gyr)	Heating rate (W kg ⁻¹)
U	1.7×10^{-8}		
U-235		0.704	5.69×10^{-4}
U-238		4.47	9.46×10^{-5}
K	3.4×10^{-5}		
K-40		1.25	2.92×10^{-5}
Th	6.8×10^{-8}	14.0	2.64×10^{-5}

1.3. Motivating questions

The thermal evolution of the interior of Mars depends on the ability of the mantle to remove heat. Core cooling is limited by the vigor of convection in the much more viscous mantle above. Here, we suggest that this efficiency may depend on the initial pre-impact conditions of Mars. In particular, we examine the effects of the pre-existing thermal state of the mantle and frequency of large impacts on the impact-induced mantle dynamics.

In the following section we describe our modeling efforts, including shock heating of the mantle due to impacts and the subsequent thermal evolution of the mantle by thermal convection. Next we present the results of the convection models with particular attention to the evolution of the thermal structure. Finally, we discuss the implications of these results on the long-term thermal evolution of Mars, and attempt to quantify the effects of uncertainties in observations of basin size and age, scaling laws, and models of shock pressure and heating.

2. Modeling

2.1. Mantle convection

We model mantle dynamics using CitcomS (Zhong et al., 2000; Tan et al., 2006), a 3D finite-element model of convection in a spherical shell. Our model contains 1.8 million elements, each with an average thickness of 26 km, and spanning 4.2° in each horizontal direction. The mantle is assumed to be viscous and incompressible, with an infinite Prandtl number, and subject to the extended Boussinesq approximation (Christensen and Yuen, 1985). Thermal convection is governed by the equations of conservation of mass, momentum and energy:

$$\nabla \cdot \vec{u} = 0$$

$$-\nabla P + \nabla \cdot [\eta(\nabla \vec{u} + \nabla^T \vec{u})] + \delta \rho g \vec{e}_r = 0 \quad (1)$$

$$\frac{\partial T}{\partial t} + \vec{u} \cdot \nabla T = \nabla \cdot (\kappa \nabla T) + H$$

where \vec{u} is velocity, P is pressure, η is dynamic viscosity, g is the gravitational acceleration, \vec{e}_r is a unit vector in the radial direction,

T is temperature, t is time, κ is the thermal diffusivity, and H is the internal heating, which includes adiabatic heating, frictional dissipation, and radioactive heat generation (Christensen and Yuen, 1985). The density varies due to temperature as $\delta\rho = \rho_0\alpha(T - T_0)$, where ρ_0 is the reference density, α is the thermal expansivity, and T_0 is the reference temperature.

We nondimensionalize Eqs. (1)–(3) using the following conversions:

$$x'_i = \frac{x_i}{R_0}, \quad u'_i = \frac{u_i}{\kappa_0/R_0}, \quad t'_i = \frac{t}{R'_0/\kappa_0}, \quad \eta' = \frac{\eta}{\eta_0}, \quad P' = P \frac{R_0^2}{\eta_0 \kappa_0},$$

$$T' = \frac{T - T_0}{\Delta T}, \quad T_S = \frac{T_0}{\Delta T}, \quad H' = H \frac{R_0^2}{\kappa_0 \rho_0 C_p \Delta T}, \quad \kappa' = \frac{\kappa}{\kappa_0} \quad (2)$$

where x_i represents a spatial coordinate, R_0 is the planetary radius, ΔT is the initial temperature difference across the mantle and C_p is the specific heat. All primed quantities are nondimensional. All '0' subscripts refer to the reference values of their respective quantities, typically chosen at the surface (though η_0 is the viscosity at the CMB). See Table 1 for the reference parameter values used in this study. Using these nondimensionalizations and dropping the primes for clarity, the momentum equation becomes:

$$-\nabla P + \nabla \cdot [\eta(\nabla \vec{u} + \nabla^T \vec{u})] + Ra T \vec{e}_r = 0 \quad (3)$$

where Ra , the Rayleigh number is defined as:

$$Ra = \frac{\rho_0 g \alpha_0 \Delta T R_0^3}{\kappa_0 \eta_0} \quad (4)$$

The nondimensional mass and energy equations are formally identical to the dimensional versions. α varies linearly with depth, decreasing by a factor of two from the surface to the CMB. The conductivity, $\kappa = \rho C_p \kappa$, varies with temperature according to an empirical relationship (Schatz and Simmons, 1972).

$$k = \begin{cases} \frac{414.8 \text{ W m}^{-2}}{30.6 \text{ K} - 0.21 T} & T < 500 \text{ K} \\ \frac{414.8 \text{ W m}^{-2}}{30.6 \text{ K} + 0.21 T} + 0.0023(T - 500 \text{ K}) & T > 500 \text{ K} \end{cases} \quad (5)$$

The mantle is cooled from above (by radiation into space), and heated from below (by secular cooling of the core) and from within by radioactive decay. The surface temperature is held constant. The CMB temperature is laterally homogeneous but varies with time as the core is cooled by the mantle. The time-dependent heating rate (Turcotte and Schubert, 2002) is given by:

$$H = 0.9928 C_0^U H^{U238} \exp \frac{t \ln 2}{\tau_{1/2}^{U238}} + 0.0071 C_0^U H^{U235} \exp \frac{t \ln 2}{\tau_{1/2}^{U235}}$$

$$+ C_0^T H^T \exp \frac{t \ln 2}{\tau_{1/2}^T} + 1.19 \times 10^{-4} C_0^K H^{K40} \exp \frac{t \ln 2}{\tau_{1/2}^{K40}} \quad (6)$$

where C_0^X is the present-day concentration of element X, H^{X1} is the heating rate of isotope X1, and $\tau_{1/2}^{X1}$ is the half-life of that isotope. The bulk concentrations (Wanke and Dreibus, 1994), half-lives, and heating rates (Turcotte and Schubert, 2002) for the long-lived

Table 3
Rheological parameters.

Parameter	Symbol	Value	Reference
Reference viscosity	η_0	10^{19} Pa s	Mitrovica and Forte (2004)
Activation energy	E	157 kJ/mol	Karato and Jung (2003)
Activation volume	V	3 cm ³ /mol	Mitrovica and Forte (2004)
Pre-exponential constant	A	1.46×10^{13} (Pa s) ⁻¹	Mitrovica and Forte (2004)

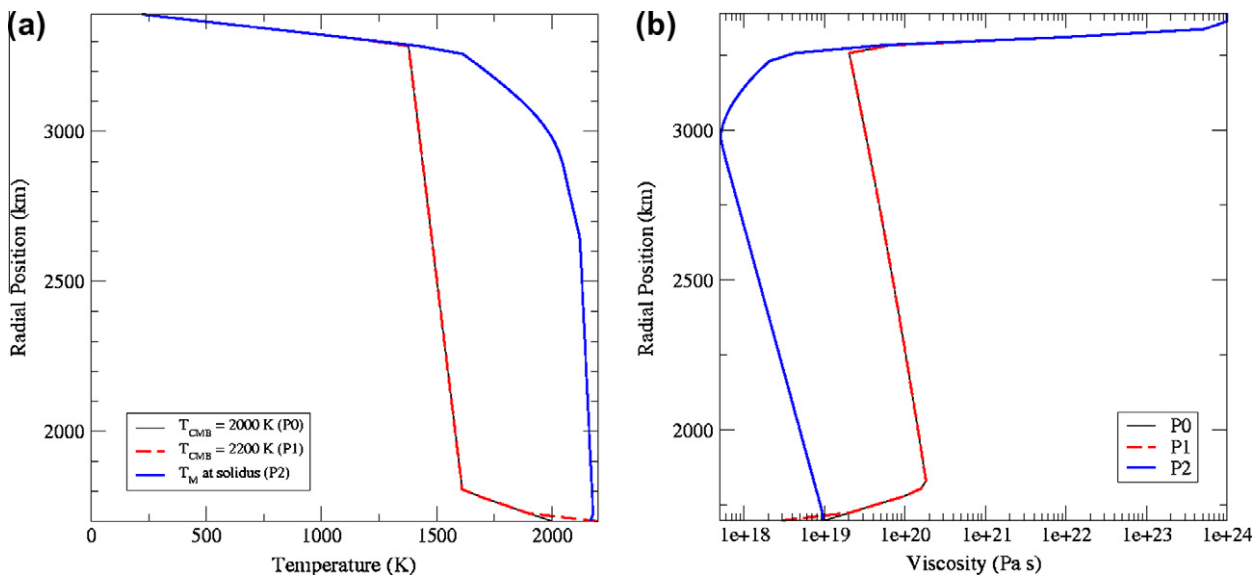


Fig. 1. Initial radial temperature (a) and viscosity (b) profiles for convection models. “Standard” case P0 (thin black curve), standard case with super-heated core P1 (dashed red curve), and interior temperature following the solidus P2 (thick blue curve).

isotopes are given in Table 2. Short-lived radioactive isotopes such as Al-26 and Fe-60 are rare after the accretionary stage of the planet and thus ignored.

The formation of the primordial crust resulting from the initial differentiation of the magma ocean will have partitioned a large fraction of the radioactive isotopes into the crust. We partition 30% of the total radioactive isotopes into the upper 50 km of the model domain (the “crust”). The remainder is distributed uniformly in the mantle. We do not otherwise model crust-mantle evolution. Variations in crustal thickness are not considered here.

We assume a Newtonian rheology with a constant grain size. The mantle viscosity depends on both temperature and pressure, according to an Arrhenius-type law.

$$\eta = A \exp \left[\frac{E + PV}{RT} \right] \quad (7)$$

where E is the activation energy, V is the activation volume, R is the gas constant, and A is a pre-exponential constant. The activation parameters (see Table 3) are chosen such that our radial viscosity structure (Fig. 1b) is consistent with that inferred for the Earth’s upper mantle based on isostatic adjustment data and convection modeling (Mitrovica and Forte, 2004; Moucha et al., 2007). The activation parameters are nondimensionalized as follows:

$$E' = \frac{E}{R\Delta T}, \quad V' = \frac{\rho_0 g R_0 V}{R\Delta T} \quad (8)$$

Using these, the rheological equation becomes:

$$\eta = \eta_0 \exp \left[\frac{E' + V'(1 - r)}{T' + T_s} - \frac{E' + V'(1 - r_c)}{1 + T_s} \right] \quad (9)$$

where r_c' is the nondimensional core radius. For numerical efficiency, the viscosity near the surface is truncated at $10^5 \eta_0$. This is sufficient to ensure a stagnant lid (Solomatov and Moresi, 1995; Harder, 2000). Higher cutoffs do not affect the results significantly, while drastically increasing the computation time. A more thorough investigation of the effects of mantle viscosity on impact-induced convection has been conducted by Ghods and Arkani-Hamed (2007).

We begin our calculations at 4.6 Ga using an initial temperature profile P0 shown in Fig. 1a (thin black line). The initial profile varies only with radius. From the surface, the temperature increases rapidly through the top thermal boundary layer (TBL). The temperature is adiabatic in the mantle interior, and then increases further in the bottom TBL. The final thicknesses of the TBLs are not known a priori, and will evolve from these initial states. We impose a small spherical harmonic degree $\ell = 20$ perturbation. In addition, we consider two alterations to the initial thermal structure, also shown in Fig. 1a. (P1) An initially super-heated core ($T_{CMB} = 2200$ K, dashed red¹ line). (P2) A warmer interior, with the temperature profile initially at the solidus (thick blue line). We allow our calculations to run for at least ~1 Gyr, or until statistically steady convection is achieved. This duration of time is more than adequate to evolve away from transient dynamics resulting from the choice of initial conditions. Note, however, that because we consider secular cooling of the core and time-dependent radioactive decay, a true steady state (as defined by constant heat flow at the surface and CMB) is never achieved.

¹ For interpretation of color in Figs. 1, 2, 4, and 7–12, the reader is referred to the web version of this article.

2.2. Shock heating from impacts

An additional effect prevents the system from reaching steady state; the introduction of heat into the interior by the Noachian basin-forming impacts. These impacts are effectively a highly localized and time-dependent source term in the energy equation. We use scaling relations to obtain the transient basin diameters D_b from the observed final basin sizes, D_b (Holsapple, 1993),

$$D_b = 1.02 D_c^{-0.086} D_{tr}^{1.086} \quad (10)$$

where D_c is the simple-to-complex transition diameter (we use 7 km for Mars; Melosh, 1989), and to obtain the projectile size D_p from the transient basins (Schmidt and Housen, 1987; Holsapple and Schmidt, 1982; Melosh, 1989),

$$D_p = 0.69 D_{tr}^{1.28} v_i^{-0.56} g^{0.28} \quad (11)$$

assuming an average impactor velocity, v_i of 10 km/s (Neukum and Wise, 1976). A significant fraction of the impactor's kinetic energy will be converted to thermal energy, raising the temperature of the interior, largely of the surrounding upper mantle.

The mantle is heated by a shock wave emanating from the impact location. The shock pressure, P_s is nearly uniform within an isobaric core, and decays rapidly with distance r outside this region (Melosh, 1989; Ahrens and O'Keefe, 1987; Pierazzo et al., 1997). Following the average model of Pierazzo et al. (1997), the shock pressure is:

$$\begin{cases} \rho_0(C + Su_c)u_c & r < r_c \\ P_s(r_c)(r_c/r)^{-1.84+2.61\log v_i} & r > r_c \end{cases} \quad (12)$$

where u_c is the particle velocity ($u_c = 0.5 v_i$; the target and projectile are assumed to have similar properties). C is the sound speed and S is a constant based on the material properties (Melosh, 1989). The radius of the isobaric core, r_c is given by:

$$r_c = 0.225 D_p v_i^{0.211} \quad (13)$$

The pressure reduction near the surface due to interference of the direct and reflected waves is taken into consideration after modifying Melosh's (1989) rectangular coordinate algorithm to a spherical coordinate algorithm. This modification has appreciable effects on the location of the interference zone, where the direct and reflected waves interfere to reduce the effective shock pressure (Louzada and Stewart, 2009).

We parameterize the impact heating as a temperature perturbation ΔT in the mantle, which is a function of the shock pressure (Watters et al., 2009). We use the foundering shock heating model of Watters et al. (2009):

$$\begin{aligned} \Delta T &= \frac{P_\delta}{2\rho_0 S C_p} (1 - f^{-1}) - (C/S)^2 (f - \ln f - 1) \\ f &= -\frac{2SP_\delta}{C^2 \rho_0} \left(1 - \sqrt{\frac{4SP_\delta}{C^2 \rho_0} + 1} \right)^{-1} \\ P_\delta &= P_s - P_0 \end{aligned} \quad (14)$$

where P_0 is the lithostatic pressure determined using a two-layered Mars model (Arkani-Hamed and Olson, 2010b).

Watters et al. (2009) assumed that all waste heat increases the temperature of the target; this premise does not take into account the latent heat of melting, which consumes a substantial amount of the waste heat. Therefore, as a modification to this method, the waste heat is assumed here to contribute to an increase in temperature up to the solidus, T_{sol} of the target material at a given pressure, after which additional temperature increase up to the liquidus, T_{liq} occurs only with partial melting (Ghods and Arkani-Hamed, 2007; Roberts and Barnouin, 2011; Ernst et al., 2010). This

temperature increase may result in a melt region several times the size of the isobaric core. However, convection is very efficient in a liquid, and the magma pond will solidify quickly compared to the dynamic timescale of the solid mantle (Reese and Solomatov, 2006). Therefore, we do not consider temperatures above T_{sol} , or production of vapor that does not further interact with the interior. Here, we do not track melting, and we restrict the temperature in the mantle to T_{sol} at all points where $T + \Delta T$ exceeds this value, in order to preserve numerical stability and avoid two-phase flow calculations.

Melt is removed to the surface. Vapor production is ignored. Partial melting may result in melt residuum of a higher viscosity than the underlying undepleted mantle. We expect that the effect of the melting on the large-scale mantle dynamics to be small for the following reasons. First, the melt region, while it may be quite large, is focused at the near surface. Prior to impact, this region is mainly in the stagnant lid, and does not participate in the convection. We do not model the transient cavity phase since the timescale for collapse is much shorter than a convective timestep. Second, while melt depletion creates an extra source of buoyancy which enhanced the upwelling of the plume, it also increases the viscosity of the solid residue which hamper the upwelling (Ghods and Arkani-Hamed, 2007), and the net effect on mantle convection will not be very large. Third, the buoyant melt migrates through the partially molten plume and ponds at the top of the plume. The strong impact weakening of the overlying lithosphere allows the melt to reach the surface more readily, such that it has only minor effects on mantle convection. Moreover, the buoyancy of the underlying solid mantle is not greatly affected by near-surface melt.

At the times given by Frey (2008) we impose the heating due to the five largest impacts, those with final basin diameters greater than 2500 km. We continue the model for approximately 1 Gyr, or until well after the final impact. For each set of model parameters, we run a corresponding "control" case in which the impact heating is not imposed.

3. Results

3.1. Effects of a single impact on mantle convective pattern

At the time of formation of the Utopia basin, we impose the appropriate impact heating on our standard background case. Fig. 2 shows the temperature increase in Mars caused by the impact that created Utopia basin. Snapshots of the temperature structure are shown in Fig. 3 for a cross-section through the impact site. The impact axis lies in the plane shown. For select frames, we also show temperature isosurfaces, viewed from both the normal to the plane of Fig. 3, and from along the impact axis. The mantle is initially convecting prior to the impact with multiple upwellings, and small-scale downwellings (Fig. 4). The impact heats a region of the mantle. Heating is strongest within a truncated sphere-shaped isobaric core and decays with distance (Figs. 3b and 4a and b). This heated region rises and spreads out, forming a thermal blanket" that insulates the mantle (Figs. 3c-f and 4c-f). An upwelling develops at the CMB, rises, and punctures the thermal blanket (Figs. 3f-g and 4e-f). The blanket ultimately dissolves, leaving a single dominant convective upwelling beneath the impact site (Fig. 3h). This convective pattern results in significant hemispheric asymmetry in the mantle temperature structure. The upwelling is relatively long lived, persisting for ~30 Myr before it starts to disorganize (Figs. 3i and 4g and h), and ~100 Myr before it disappears entirely (Fig. 3j-l). Fig. 3 with some additional frames can be viewed as an animation in the Supplementary Material.

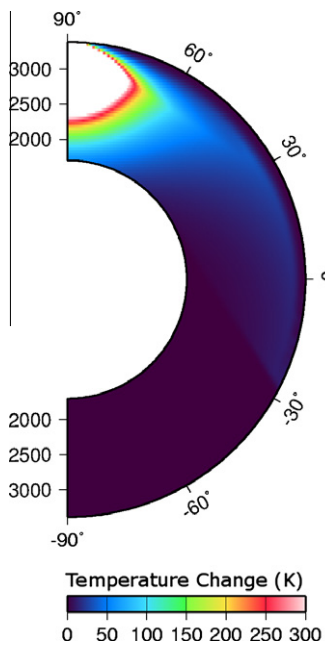


Fig. 2. Temperature change due to impact heating from Utopia (before taking melting into account) in a slice through the impact axis. The heating from a single impact is axisymmetric about this axis (assuming a vertical impact). Color scale saturates at $\Delta T = 300$ K, but the temperature increase is considerably higher (up to 3600 K) in the isobaric core.

Compared with the background model, the impact heating causes a rapid, initial increase in surface heat flux. The bulk of

the impact heating is deposited at some depth, so the effect on the surface heat flux is not immediately seen. The resulting buoyancy and spreading of the heated region results in continued increase in the surface heat flux over the next ~ 100 Myr, the effective lifetime of the plume. As the plume dissipates and the thermal pulse diffuses through the stagnant lid, the heat flux trends back towards the non-impact level. However, total recovery does not occur. The change in convective planform results in a long-term elevation in total surface heat flow of a few percent. This global heat flow evolution is shown in Fig. 5. Vertical lines mark the times of the later snapshots shown in Fig. 3 (a-f are compressed into the earliest line). Note that even the non-impact case is not in steady state. The small initial rise in heat flux is the last phase of evolving from the initial condition. The subsequent decrease results from a reduction in internal heating caused by the decay of radioactive heat sources.

The heat flux has extreme lateral variations, however. Fig. 6 shows a polar-projection map view of the heat flux at the surface at the same times as for the snapshots shown in Fig. 3, with the impact site at the center of each frame. Prior to impact, the pre-existing convective structure results in relatively small regions of elevated surface heat flux (Fig. 6a). The impact introduces a small region of strongly elevated heat flux at the center of the impact site where near-surface heating is deposited (Fig. 6b). The heat flux increases as more heat from the initially heated region (e.g. Fig. 3b) diffuses upward through the stagnant lid (Fig. 6c-h). Meanwhile, in the underlying mantle, the heated region spreads out beneath the stagnant lid. As the heat from this thermal blanket diffuses upward, the elevated heat flux is spread over a much greater region (Fig. 6i-l). The presence of the stagnant lid causes the pattern of surface heat flux to lag the corresponding convective pattern by

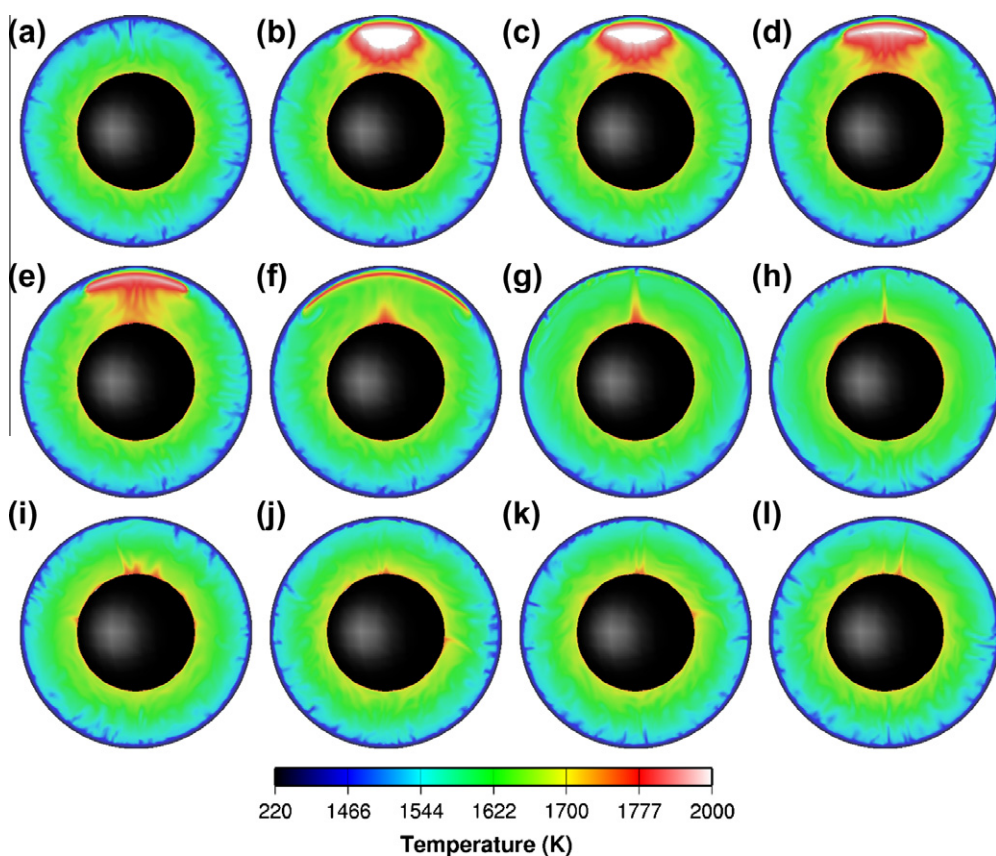


Fig. 3. Temperature structure on cross-section of the mantle though the impact site immediately before (a) and after (b) the impact, after 30 ky (c), 60 ky (d), 120 ky (e), 850 ky (f), 5.7 Myr (g), 23 Myr (h), 53 Myr (i), 107 Myr (j), 134 Myr (k) and 582 Myr (l). The normal to the plane shown (0°N , 26°E) is perpendicular to the impact axis.

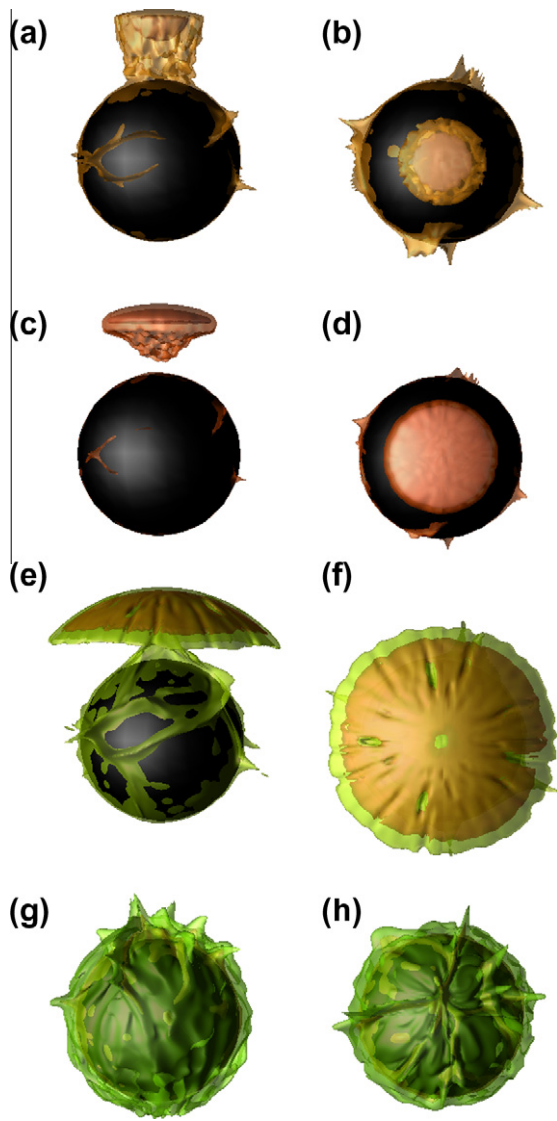


Fig. 4. Plots of temperature isosurfaces corresponding to select frames in Fig. 3. The rows correspond to Fig. 3b, d, f, and i respectively. The left column is from the same angle as in Fig. 3. The right column is from directly above the impact site. Isosurfaces shown are 1750 K and 1910 K (a–d); 1680 K and 1790 K (e and f); 1560 K and 1660 K (g and h). In all cases, the warmer surface is the redder, innermost one.

tens of Myr. Note that while the impact heating is symmetric about the impact axis, the subsequent heat flow is not, due to the pre-existing thermal structure. The post-impact heat flow pattern mimics the pre-existing pattern, though the magnitude is greatly increased.

The high temperature region in the upper mantle increases the vigor of convection. This can be illustrated by examining the evolution of the total kinetic energy, E_k , of the mantle over time (see Fig. 7). The kinetic energy is computed:

$$E_k = \frac{1}{2} \rho_0 \int_V |u|^2 dV \quad (15)$$

where $|u|$ is the velocity at a given point, and dV is the volume element. Upon impact, the newly buoyant region causes the rms velocity of the mantle to be dramatically increased. This enhanced convective vigor lasts for roughly 50 Myr before returning to the pre-impact level. The increased velocities are largely confined to the hemisphere in which the impact occurs, though the velocities

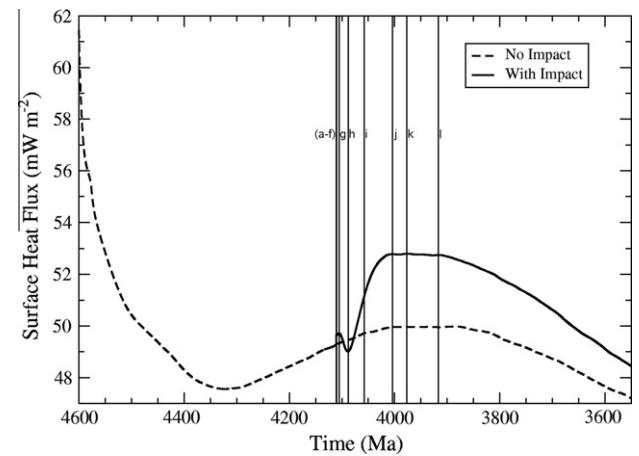


Fig. 5. Evolution of the average surface heat flow for Mars models with (solid line) and without (dashed line) a Utopia-sized impactor. Vertical lines marked with letters denote the times and frames of the corresponding temperature plot in Fig. 3. Frames a–f are compressed into the left-most vertical line.

in the other hemisphere are also enhanced to a lesser extent (note the logarithmic scale on the vertical axis).

3.2. Effects of impactor size on heat flow anomaly

We have run an additional set of models investigating the effects of different size impacts in isolation in order to evaluate the dependence of the magnitude of the heat flow anomaly and the recovery timescale on projectile size. We have run three models based on our standard (P0) mantle model in which we include only the heating from a small basin (Hematite), a medium sized basin (Hellas), or a large basin (Utopia). Fig. 8 shows the time evolution of the surface heat flux anomalies (that is, the difference in heat flux between each model and P0) resulting from each impact.

We observe that the magnitude and timing of heat flow anomalies scale with basin size. We note that these relationships are based on only a few models and are thus extremely tentative. We present them to give a general sense of how impact size affects heat flux and recovery time, but at this level of fidelity we do not recommend they be used as scaling laws.

The magnitude of the heat flux anomalies scales strongly with the size of the impactor. Using a least-squares approximation, we find that the peak heat flux anomaly (in mW m^{-2}) scales with final basin size (in 1000 km) as:

$$\delta F \propto D^{2.66} \quad (16)$$

The time delay between the impact event and the peak heat flux anomaly also scales with basin size, primarily because the heating is deposited deeper in the mantle. This scaling is linear. The timescale for heat flux to return to pre-impact level, however, scales much more weakly. Decay in the heat flux anomaly is initially much swifter for the larger impacts, but all models return to the pre-impact level after approximately the same time.

3.3. Effects of pre-existing convective pattern

We have investigated the effects of pre-existing convective structure on the response to impact heating. Here we placed a Utopia-forming impactor over a convective upwelling, over a downwelling, and over a quiescent region. Fig. 9 shows the evolution of the surface heat flux for each of these cases. The behavior is similar in all cases except for the timing. The pre-existing convective motion can either aid or hinder the recovery. Counterintuitively, the peak heat flux is reached fastest when the impact is placed over a pre-existing downwelling rather than over an upwelling, and that

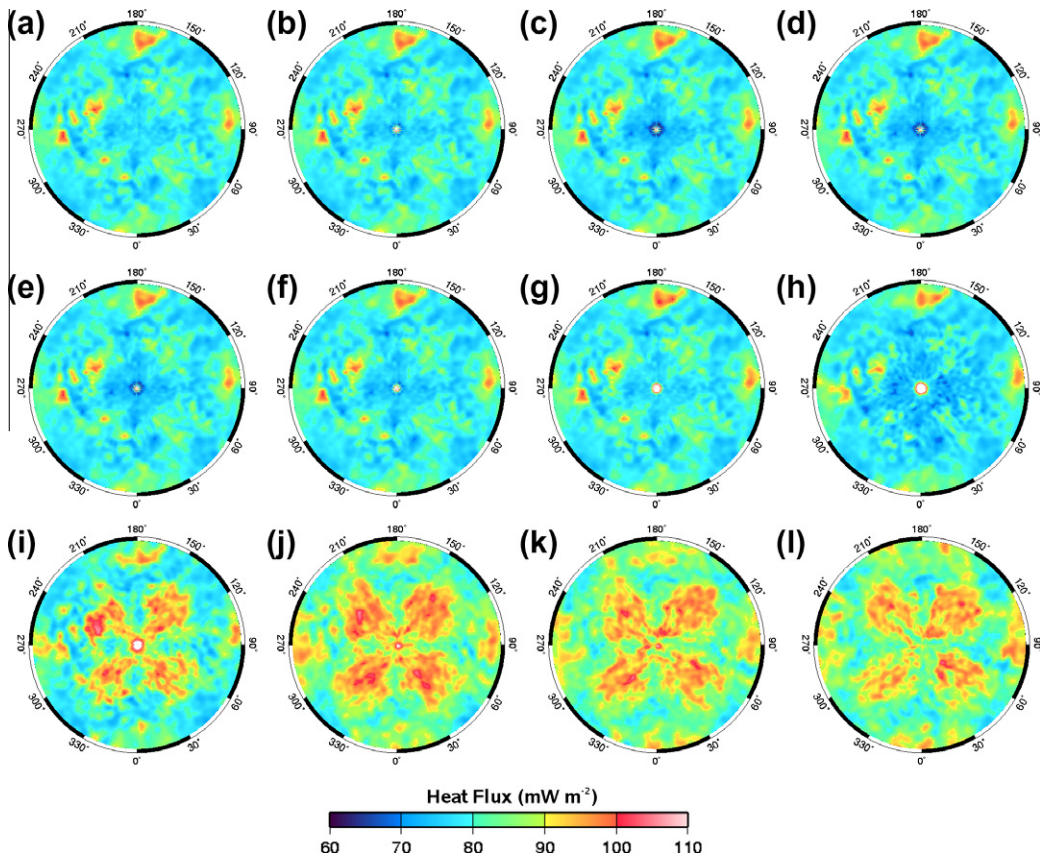


Fig. 6. Maps of the total heat flux at the surface at the times corresponding to the frames in Fig. 3 and the vertical lines in Fig. 5. Note that while the impact heating is symmetric about the impact axis, the subsequent heat flux is not, due to the pre-existing thermal structure (e.g. panel a).

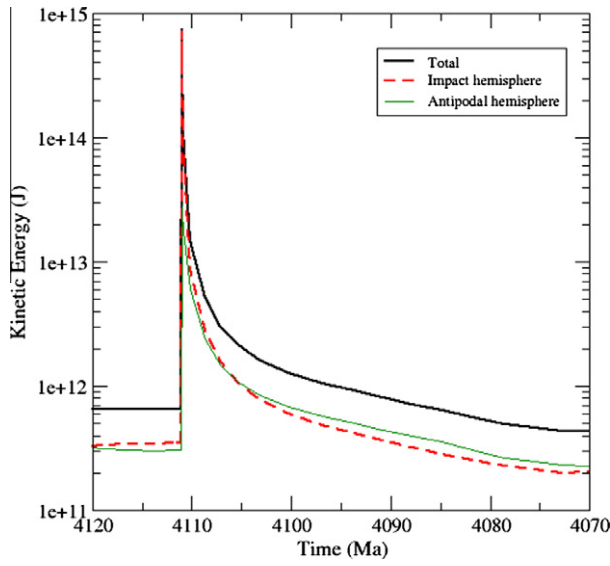


Fig. 7. Evolution of the kinetic energy in the mantle shortly before and after the Utopia impactor. Shown are the total kinetic energy (thick black line), kinetic energy in the impact hemisphere (dashed red line), and kinetic energy in the hemisphere antipodal to the impact (thin green line). Note the logarithmic scale on the vertical axis.

the maximum heat flux is highest in the former case. This can be explained by the fact that the impact has now introduced a new region of upwelling in addition to the pre-existing regions, rather than merely adding to an already existing upwelling. The

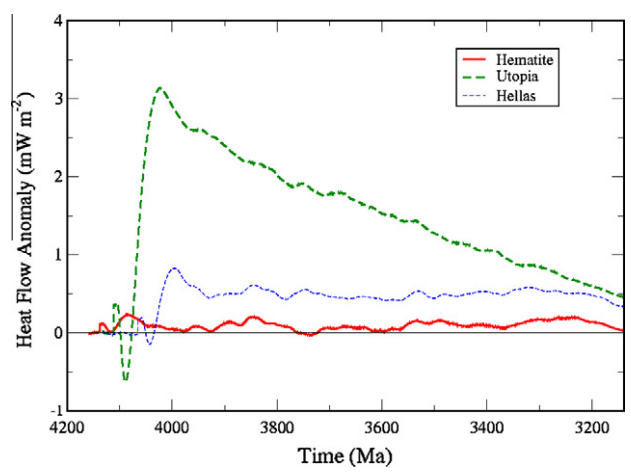


Fig. 8. Heat flow anomaly (i.e. the difference in heat flow from a comparable case with no impact heating) for three different single impacts.

upwelling and downwelling impact cases are not truly symmetrical. Because the rheology is strongly temperature and pressure dependent, the long-wavelength convective pattern is dominated by upwellings. Downwellings are all in much smaller “drips” off the stagnant lid, and the removal of one of them has only a minor effect on the mantle dynamics in comparison to the large perturbation introduced by the impact itself. We find that the pre-existing convective pattern has only a minor effect on the thermal evolution of the mantle in response to the impact, affecting the maximum heat flux perturbation and timing by no more than

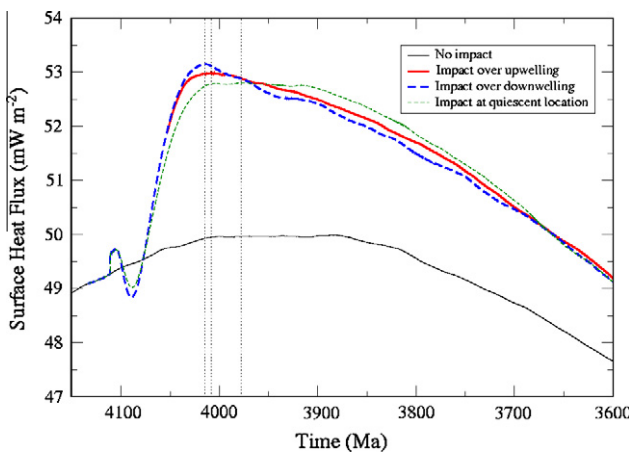


Fig. 9. Surface heat flow evolution in response to Utopia-forming impacts at different locations with respect to the preexisting convective structure. Dotted vertical lines denote the times of peak heat fluxes for the downwelling, upwelling, and quiescent cases (from left to right).

~10%. We note that in all cases there is some long-term alteration to the heat flow.

3.4. Sequence of basin-forming impacts

We investigated the cumulative effects of multiple impacts on the mantle dynamics. At the times and relative locations of the twenty largest impacts (Frey, 2008 and Table 4), we imposed the heating due to the respective impacts. Only the very largest impacts (forming basins with $D_b > 2500$ km) can significantly heat the lower mantle (Roberts et al., 2009). Therefore, we also ran a similar model with only the five largest impacts. The evolution of heat flux for these models is shown in Fig. 10. We find that the top five impacts account for the majority (~80%) of the heat flow anomalies. We also find that due to the aforementioned lag between a perturbation in the mantle temperature and the peak perturbation in the surface heat flux, it is difficult to identify the heat flux increases that are due to each impact. The initial rise in heat flux can be seen relatively easily (vertical lines in Fig. 10 are shown for the five largest impacts). The mean interval between the largest impacts is around 25 Myr, which is considerably shorter than the ~100 Myr before the full heat flux anomaly from a single impact appears at the surface (see e.g. Fig. 6). This suggests that multiple impacts indeed have a cumulative effect on the long term thermal structure of the martian interior.

3.5. Effects of initial conditions

The initial temperature profile for the martian interior is not well known (by “initial”, we refer to the starting point for our models at a model age of 4.6 Gyr, and after solidification of any magma ocean). Therefore, in addition to the standard case (P0) presented above (Fig. 1), we have examined two additional models. The first (P1) is identical to P0 in the top thermal boundary layer and in the interior, but has a core temperature that is 200 K hotter. The second (P2) temperature profile follows the dry peridotite solidus (McKenzie and Bickle, 1988) below the stagnant lid, and has a CMB temperature similar to that in P1. For each temperature profile we ran convection models in which we included the heating from the five largest impacts at their times of formation. We also ran control models without impact heating. Fig. 11 shows the evolution of surface heat flux for all three temperature profiles. The choice of initial core temperature does not dramatically alter the

Table 4
Giant Noachian impact basins on Mars (after Frey (2008) and Roberts et al. (2009)).

Name	Abbrev.	Long. (°E)	Lat. (°N)	Diam. (km)	Model age (Ma)
Amenthes	Am	110.6	-0.9	1070	4218
Zephyria	Ze	164.3	-12.4	1193	4210
Daedalia^a	Da	228.3	-26.5	2639	4199
Sirenum	Si	205.3	-67.4	1069	4196
SW Daedalia	SW	213.9	-29.4	1278	4176
Ares^a	Ar	343.9	4.0	3300	4167
Amazonis^a	Az	187.9	27.1	2873	4154
In Amazonis	IA	192.5	29.3	1156	4152
Solis	So	275.3	-23.8	1663	4148
N Tharsis	NT	243.6	17.6	1347	4143
Chryse	Cr	318.0	25.0	1725	4140
Hematite	Hm	357.8	3.2	1065	4138
Scopolus	Sc	81.8	6.9	2250	4133
Acidalia^a	Ac	342.7	59.8	3087	4132
North Polar	NP	195.2	80.0	1600	4124
Utopia^a	Ut	115.5	45.0	3380	4111
SE Elysium	SE	170.3	3.7	1403	4107
Hellas	He	66.4	-42.3	2070	4065
Argyre	Ag	317.5	-49.0	1315	4043
Isidis	Is	87.8	13.4	1352	3810

^a Denotes five largest basins.

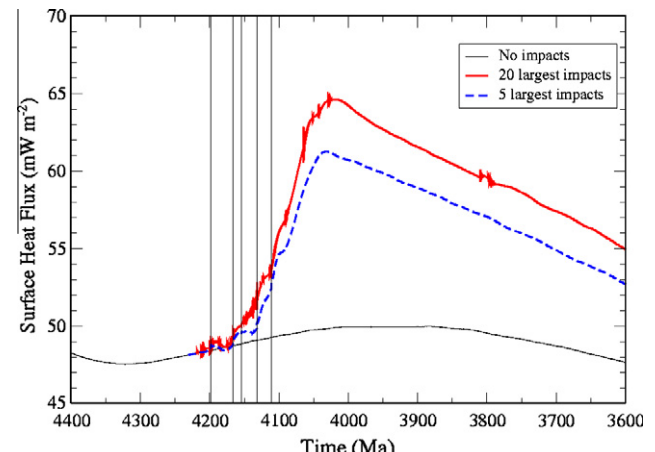


Fig. 10. Evolution of the surface heat flow in response to heating by the five largest and 20 large impacts. Vertical lines mark the five largest impacts.

results; difference in the surface heat flux is only a few percent. The case with the mantle temperature initially at the solidus is quite different however. The impact heating has a relatively modest effect. Although some cooling has occurred prior to the impacts, the interior temperature is still very warm. Thus, the impact heating returns the mantle to the solidus with a relatively small change in temperature, and most of the energy goes into melt production. As discussed above, we do not track the melt or consider super-solidus temperatures here. Because the molten region solidifies quickly compared to the convective timescale, energy in excess of that required to bring the mantle to the solidus does not participate in the mantle dynamics. The impact heating in this case does not really elevate the heat flux, but delays its decrease by ~150 Myr. We do not believe such a model is geologically likely, partly because the mantle remains warm for an extended period due to radioactive heating. The evolution of the horizontally averaged temperature for this case is shown in Fig. 12. While there is some initial cooling during the first ~50 Myr, the temperature remains near the solidus for an extended period and requires nearly 2 Gyr to cool to even the hottest transient temperature reached by our standard model (see Fig. 1).

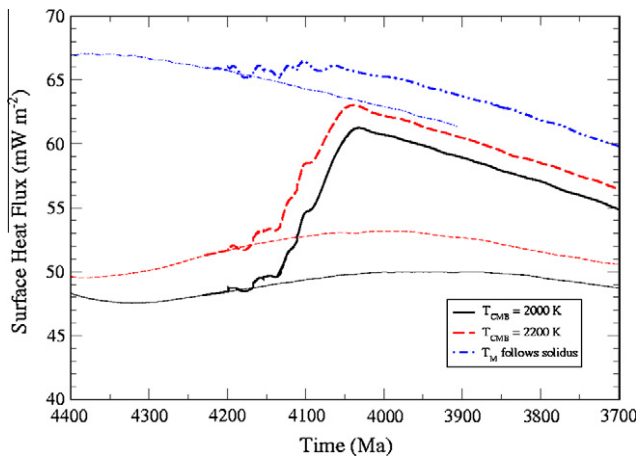


Fig. 11. Surface heat flux with (thick curves) and without (thin curves) impact heating from five largest impact basins for three different initial temperature profiles.

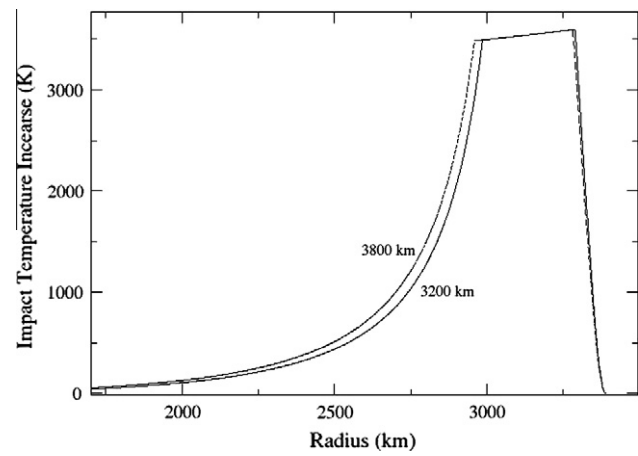


Fig. 13. Temperature increase directly beneath the impact site resulting from heating by impacts forming basins with diameters of 3200 km (solid curve) and 3800 km (dashed curve). The principal difference between models is the size of the isobaric core. Curves shown in this plot assume all waste heat goes into increasing temperature, according to the Foundering shock model of Watters et al. (2009). Energy consumed by the latent heat of melting will reduce the amplitude, but will not affect the general shape.

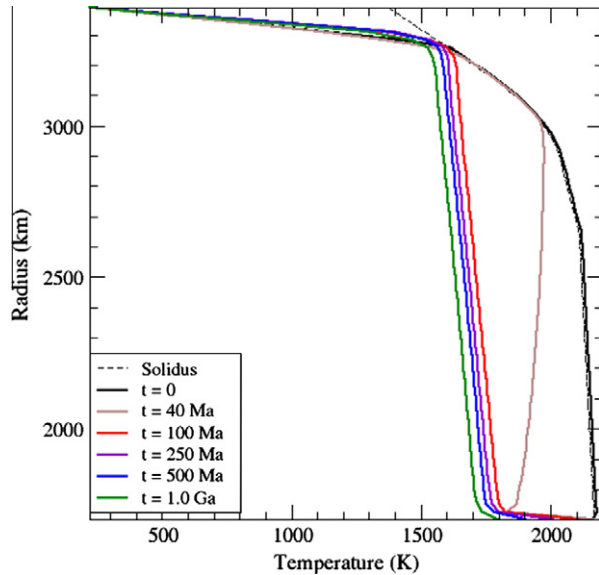


Fig. 12. Evolution of the horizontally-averaged temperature, initially at the solidus beneath the stagnant lid. Rapid cooling occurs in the first 50 Myr, but the temperature is still elevated above the initially cooler cases for an extended period.

4. Discussion

Roberts et al. (2009) exposed a possible connection between the observed giant impact basins on Mars (Frey, 2008) and thermal changes in the deep interior. In particular, the goal of Roberts et al. (2009) was to address the coincidental timing between the basin formation and the disappearance of the global magnetic field at the same time (Lillis et al., 2008), and the focus was on the impact-induced thermal perturbations at the CMB. A key finding from that study was the importance of the interval between large impact events relative to the time needed for the mantle to dissipate a given perturbation.

Here, we have shown that the timing for dissipation of impact heating is controlled by the initial thermal state of the mantle and core, and the pre-existing convective structure in the vicinity of the impact. Here we also focus on surface heat flux as a more robust measure of the departure from pre-impact state, since this does not involve feedback between core and mantle thermal

models. However, there are many reasons that the results presented in this paper should be regarded as rough estimates, obtained on the basis of existing information, and have qualitative importance. Here we briefly discuss major sources of uncertainties and provide a rough estimate of the effects of each uncertainty.

4.1. Basin size

Although we use those of Frey (2008) largely because the measurement method is the same for all of the basins, the sizes of some of the giant basins have been estimated by many authors. As an example, we consider multiple estimates for the size of the largest basin, Utopia. Thomson and Head (2001) suggested a mean circular basin of 3200 km in diameter, while Frey's (2008) measurement led to an average diameter of 3380 km. Using a spherical harmonic membrane-flexural model, Andrews-Hanna and Zuber (2010) inverted the gravity and topography of Mars to estimate the pre-fill basin topography and concluded that Utopia is highly elliptical with an isostatic root of 2000 km by 2400 km. The isostatic root probably underestimates the size of a giant impact basin partly because the modifications subsequent to the collapse of the transient cavity may not have appreciable effects on the root, while significantly increase the basin diameter. In the present study we used Frey's diameter of 3380 km. We also run a model with the basin diameter of 3200 km. Fig. 13 compares the temperature profiles along the axis of symmetry directly beneath the impact site for the two models. Reducing the diameter from 3380 km to 3200 km decreases the radius of the isobaric core from 216 km to 202 km but has no effect on the temperature in this region, while slightly decreasing the temperature in the deeper parts.

4.2. Scaling laws

The formation mechanism of giant basins is still a matter of debate. The scaling law of Holsapple (1993) that we have adopted provides rough estimates of their transient diameters. The post-impact collapse of a giant impact basin is largely controlled by dynamic weakening along impact-induced faults (e.g. Senft and Stewart, 2009) and the transient diameter of the basin is likely

closer to its final diameter than that obtained from the scaling laws. Many of the giant impacts are oblique, while we have assumed vertical impacts resulting in circular basins in accordance with the scaling law we have adopted. Although the surface morphology of an oblique impact differs significantly from that of a vertical impact, the shock pressure distribution at far distances from the impact site seems to be less sensitive to the impact angle relative to horizon (Pierazzo and Melosh, 2000), especially when the angle is larger than 30 degrees (Elbeshausen et al., 2009).

4.3. Impact interval

Another source of uncertainty is the impact ages. These are based on crater counts, and the ages estimated by Frey (2008) are within \pm a few tens of Myr. We have used the average ages of the impacts. However, considering the error bars of the age values, it is possible that some of the giant impacts, such as Acidalia and Utopia have occurred at a very short time period, almost simultaneously. Such an event will have considerable effects on mantle dynamics. We have run a model where Utopia and Acidalia occurred simultaneously. Snapshots of the temperature structure in response to the double impact are shown in Fig. 14. Initially two heated regions form, one associated with each impact basin. During the rising and spreading phase the thermal blankets nearly merge, though they do force a temporary downwelling at the interface. Later, a single upwelling region develops at the CMB between the two impact sites. The timescales are similar to the single impact case.

4.4. Shock pressure distribution

There are vast differences among the shock pressure distribution models outside the isobaric core proposed by several investigators. We have adopted the average model of Pierazzo et al. (1997). Fig. 15 shows several shock pressure distribution models outside the isobaric core created by a Utopia-type impactor with an impact velocity of 10 km/s. The pressure in the isobaric core is the same among the models, but that outside differ substantially. This is even the case for the model by Pierazzo et al. (1997) when the variances of the parameters are taken into consideration.

4.5. Shock heating model

Watters et al. (2009) investigated three different shock heating models, namely “ordinary”, “foundering” and “climbing”. The ordinary model adopts a uniform density mantle and assumes that the pre-shocked material is at zero pressure in the Hugoniot equations, whereas the foundering model corrects for the lithostatic pressure in the equations. The climbing model accounts for the changes in the Hugoniot equations due to lithostatic pressure and depth-dependent density in the mantle. Although this mechanism is more realistic, it requires a viable density model of the planet at about 4 Ga, which is not well constrained. For this reason we adopted the foundering model. The ordinary model significantly overestimates the impact temperature increase (Watters et al., 2009, personal communication), whereas the foundering model tends to underestimate the temperature increase (though to a

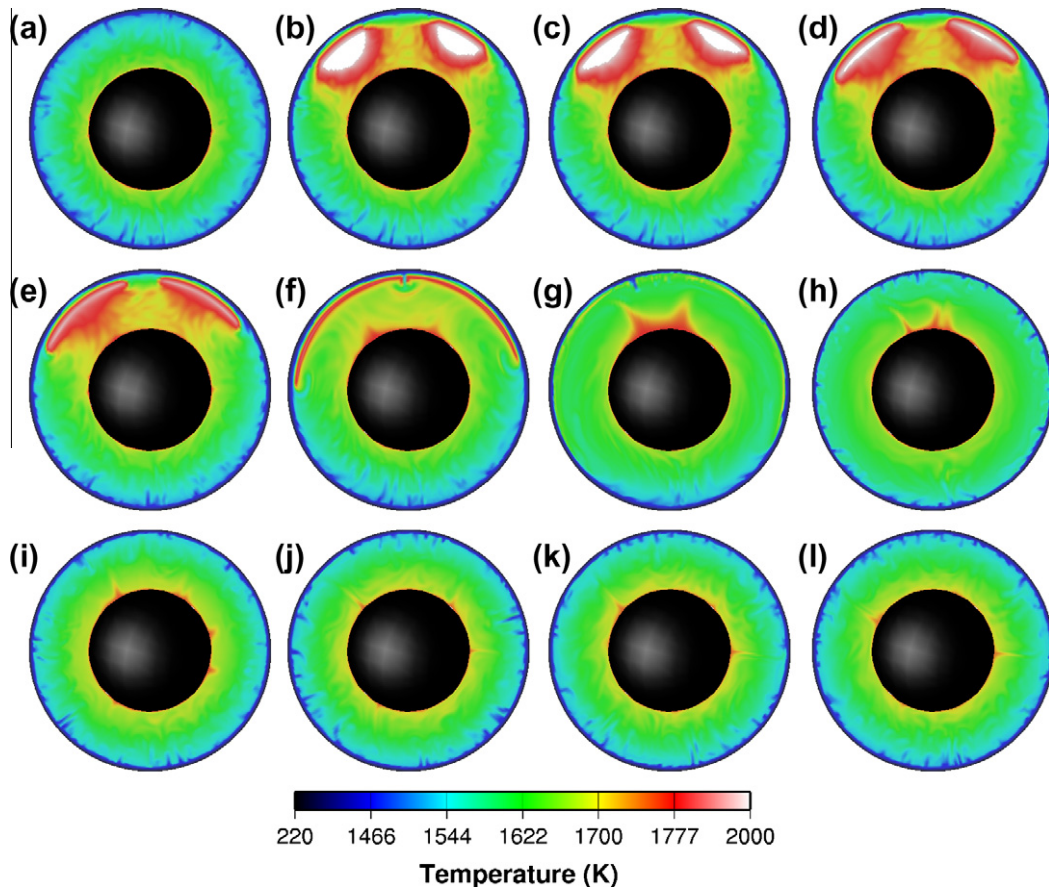


Fig. 14. Temperature after impacts forming Acidalia and Utopia basins simultaneously. Slice through the centers of both basins shown for the same timesteps as in Fig. 3. The normal to the plane shown (15° S, 42° E) is perpendicular to both impact axes.

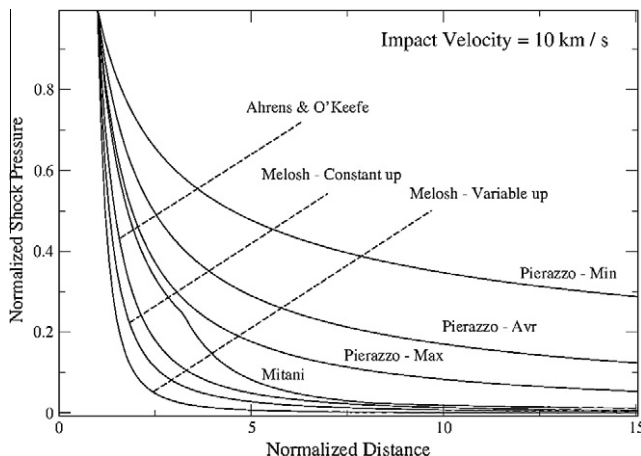


Fig. 15. Comparison of models for distribution of shock pressure with distance from the isobaric core, normalized to its radius. All curves are for an impact at 10 km/s. Shown are the shock pressure computed using the average parameters (Pierazzo – avr), from Pierazzo et al. (1997), as used in this study, as well as the extremes of the error bars from that study (Pierazzo – Min and Pierazzo Max). Also shown are results from Ahrens and O'Keefe (1987), Mitani (2003), and from Melosh (1989), using both constant (Melosh – Constant up) and variable (Melosh – variable up) particle velocities.

lesser degree). The temperature increase by the climbing model is between these two extremes, but is better approximated by the foundering model (see Fig. 2 of Watters et al. (2009)).

4.6. Outstanding questions

Following Roberts et al. (2009), we have not included direct impact heating of the core, under the assumption that since motion in the fluid core is much faster than in the mantle, any lateral heterogeneity in temperature could not be maintained. However, radial variations may persist (e.g. Arkani-Hamed and Olson, 2010a,b), resulting in a stably stratified core, and reducing the heat flow anomaly. Furthermore, the low specific heat of the core may result in a stronger increase in core temperature than in the overlying mantle, which may increase the CMB heat flow. However, heat removal from the deeper parts of the core is still severely restricted, and dynamo activity is inhibited. An additional consideration is that of melt production and migration. Planetary impacts produce vast quantities of melt (Melosh, 1989); in the case of basin-forming impacts, the melt volume produced in the first Gyr by direct impact melt and subsequent melting of the mantle (Arkani-Hamed and Ghods, 2011) may be several times that of the isobaric core (Pierazzo et al., 1997). In the current study, we have partitioned the impact heating into temperature increase and melt production, but have assumed that the melt does not affect the mantle convection significantly. That is, we have not modeled melt extraction, or considered compositional and rheological variations in the solid residuum. The melt itself is buoyant assumed to be extracted to the surface on a rapid timescale in the present study, and thus does not participate further in the convection. These issues will be addressed with in future work in which we model thermochemical convection in the mantle (e.g. Roberts and Barnouin (2011)), and couple the 3D mantle models to parameterized 1-D models of core cooling.

5. Conclusions

We draw the following conclusions from our modeling of impact heating of Mars and the mantle convection triggered by the heating:

1. A single basin-forming impact fundamentally affects the flow field of the mantle in the entire hemisphere near the impact. Besides producing a very hot buoyant isobaric region in the upper mantle, such an impact promotes the formation of an upwelling at the base of the mantle directly under the impact site, resulting in long-lived (~ 100 Myr) single-plume convection. This pattern is altered if another similar-sized impact occurs within this time frame.
2. The time for the heat flow to recover from a single impact (~ 100 Myr, though this depends on the viscosity) exceeds the interval between the largest basin-forming impacts (~ 25 Myr). Therefore, cumulative effects of multiple impacts are expected.
3. The alteration of the mantle dynamics is dominated by the five largest basin-forming impacts ($D > 2500$ km). The impacts that formed the remaining basins ($1000 \text{ km} < D < 2500 \text{ km}$) have a second-order effect. The magnitude of the heat flow anomaly scales roughly with the final basin diameter to the power of $8/3$.

Acknowledgments

We thank two anonymous reviewers whose constructive reviews strengthened the paper. This work has been supported by a postdoctoral fellowship to JHR from the Johns Hopkins University Applied Physics Laboratory, and by Natural Sciences and Engineering Research Council of Canada (NSERC) fund to JAH. Calculations performed here were supported by code from the Computation Infrastructure for Geodynamics and by the UCSC Astrophysics supercomputing cluster *pleiades*.

Appendix A. Supplementary data

Supplementary data associated with this article can be found, in the online version, at doi:10.1016/j.icarus.2011.11.038.

References

- Acuña, M.H. et al., 2001. Global distribution of crustal magnetization discovered by the Mars global surveyor MAG/ER experiment. *J. Geophys. Res.* 106, 23403–23417.
- Ahrens, T.J., O'Keefe, J.D., 1987. Impact on the Earth, ocean and atmosphere. *Int. J. Impact Eng.* 5, 13–32.
- Andrews-Hanna, J.C., Zuber, M.T., 2010. Elliptical craters and basins on the terrestrial planets. *Geol. Soc. Am. Spec. Pap.* 465, 1–13.
- Arkani-Hamed, J., Ghods, A., 2011. Could giant impacts cripple core dynamos of small terrestrial planets? *Icarus* 212, 920–934.
- Arkani-Hamed, J., Olson, P., 2010a. Giant impact stratification of the martian core. *Geophys. Res. Lett.* 37, L02201.
- Arkani-Hamed, J., Olson, P., 2010b. Giant impacts, core stratification, and failure of the martian dynamo. *J. Geophys. Res.* 115, E07012.
- Arkani-Hamed, J., Seyed-Mahmoud, B., Aldridge, K.D., Baker, R.E., 2008. Tidal excitation of elliptical instability in the martian core: Possible mechanism for generating the core dynamo. *J. Geophys. Res.* 113, E06003. doi:10.1029/2007JE002982.
- Bills, B.G., Ferrari, A.J., 1978. Mars topography, harmonics, and geophysical implications. *J. Geophys. Res.* 83, 3497–3508.
- Christensen, U.R., Yuen, D.A., 1985. Layered convection induced by phase transitions. *J. Geophys. Res.* 90, 10291–10300.
- Cohen, B.A., Swindle, T.D., Kring, D.A., 2000. Support for the Lunar Cataclysm Hypothesis from Lunar Meteorite Impact Melt Ages. *Science* 290, 1754–1755.
- Elbeshausen, D., Wunnemann, K., Collins, G.S., 2009. Scaling of oblique impacts in frictional targets: Implications for crater size and formation mechanisms. *Icarus* 204, 716–731. doi:10.1016/j.icarus.2009.07.018.
- Ernst, C.M., Murchie, S.L., Barnouin, O.S., Robinson, M.S., Denevi, B.W., Blewett, D.T., Head, J.W., Izenberg, N.R., Solomon, S.C., Roberts, J.H., 2010. Exposure of spectrally distinct material by impact craters on Mercury: Implications for global stratigraphy. *Icarus* 209, 210–223. doi:10.1016/j.icarus.2010.05.022.
- Esposito, P.B. et al., 1992. Gravity and topography. In: Kieffer, H.H. et al. (Eds.), *Mars*. Univ. of Arizona Press, Tucson, pp. 209–248.
- Frey, H.V., 2008. Ages of very large impact basins on Mars: Implications for the Late Heavy Bombardment in the inner Solar System. *Geophys. Res. Lett.* 35, L13203. doi:10.1029/2008GL033515.

- Ghods, A., Arkani-Hamed, J., 2007. Impact-induced convection as the main mechanism for formation of mare basalts. *J. Geophys. Res.* 112, E03005. doi:10.1029/2006JE002709.
- Gomes, R., Levison, H.F., Tsiganis, K., Morbidelli, A., 2005. Origin of the cataclysmic Late Heavy Bombardment period of the terrestrial planets. *Nature* 435, 466–469.
- Harder, H., 2000. Mantle convection and the dynamic geoid of Mars. *Geophys. Res. Lett.* 27, 301–304.
- Hartmann, W.K., Neukum, G., 2001. Cratering chronology and the evolution of Mars. *Space Sci. Rev.* 96, 165–194.
- Hauck, S.A., Phillips, R.J., 2001. Thermal and crustal evolution of Mars. *J. Geophys. Res.* 107, 5052. doi:10.1029/2001JE001801.
- Holsapple, K.A., 1993. The scaling of impact processes in planetary sciences. *Ann. Rev. Earth Planet. Sci.* 21, 333–373.
- Holsapple, K.A., Schmidt, R.M., 1982. The Scaling of Impact Processes in Planetary Sciences. *J. Geophys. Res.* 87, 1849–1870.
- Karato, S., Jung, H., 2003. Effects of pressure on high-temperature dislocation creep in olivine. *Philos. Mag.* 83, 401–414.
- Lillis, R.J. et al., 2008. Rapid decrease in martian crustal magnetization in the Noachian era: Implications for the dynamo and climate of early Mars. *Geophys. Res. Lett.* 35, L14203.
- Louzada, K.L., Stewart, S.T., 2009. Effects of planet curvature and crust on the shock pressure field around impact basins. *Earth Planet. Sci. Lett.* 286, L15203. doi:10.1029/2009GL037869.
- McKenzie, D., Bickle, M.J., 1988. The volume and composition of melt generated by extension of lithosphere. *Petrol. J.* 29, 625–679.
- Melosh, H.J., 1989. Impact Cratering. Oxford Univ. Press, London, 253pp.
- Mitani, N.K., 2003. Numerical simulations of shock attenuation in solids and reevaluation of scaling law. *J. Geophys. Res.* 108 (E1), 5003. doi:10.1029/2000JE001472.
- Mitrovica, J.X., Forte, A.M., 2004. A new inference of mantle viscosity based upon joint inversion of convection and glacial isostatic adjustment data. *Earth Planet. Sci. Lett.* 225, 177–189.
- Monteux, J.N., Coltice, N., Dubuffet, F., Ricard, Y., 2007. Thermomechanical adjustment after impacts during planetary growth. *Geophys. Res. Lett.* 34, L24201. doi:10.1029/2007GL031635.
- Moucha, R., Forte, A.M., Mitrovica, J.X., Daradich, A., 2007. Lateral variations in mantle rheology: Implications for convection related surface observables and inferred viscosity models. *Geophys. J. Int.* 169, 113–135.
- Neukum, G., Wise, D.V., 1976. Mars: A standard crater curve and possible new time scale. *Science* 194, 1381–1387.
- Nimmo, F., Stevenson, D.J., 2000. Influence of early plate tectonics on the thermal evolution and magnetic field of Mars. *J. Geophys. Res.* 105, 11969–11979.
- Pierazzo, E., Melosh, H.J., 2000. Melt production in oblique impacts. *Icaurs* 145, 252–261.
- Pierazzo, E.P., Vickery, A.M., Melosh, H.J., 1997. A reevaluation of impact melt production. *Icarus* 127, 208–223.
- Reese, C.C., Solomatov, V.S., 2006. Fluid dynamics of local martian magma oceans. *Icarus* 184, 102–120. doi:10.1016/j.icarus.2006.04.008.
- Reese, C.C., Solomatov, V.S., Baumgardner, J.R., 2002. Survival of impact-induced thermal anomalies in the Martian mantle. *J. Geophys. Res.* 107, 5082. doi:10.1029/2000JE001474.
- Roberts, J.H., Barnouin, O.S., 2011. The effect of the Caloris impact on the mantle dynamics of Mercury. *J. Geophys. Res.*, in press.
- Roberts, J.H., Zhong, S., 2004. Plume-induced topography and geoid anomalies and their implications for the Tharsis Rise on Mars. *J. Geophys. Res.* 109, E03009. doi:10.1029/2003JE002226.
- Roberts, J.H., Lillis, R.J., Manga, M., 2009. Giant impacts on early Mars and the cessation of the martian dynamo. *J. Geophys. Res.* 114, E04009.
- Schatz, J.F., Simmons, G., 1972. Thermal conductivity of Earth material at high temperatures. *J. Geophys. Res.* 77, 6966–6983.
- Schmidt, R.M., Housen, K.R., 1987. Some recent advances in the scaling of impact and explosion cratering. *Int. J. Impact Eng.* 5, 543–560.
- Senft, L.E., Stewart, S.T., 2009. Dynamic fault weakening and the formation of large impact craters. *Earth Planet. Sci. Lett.* 287, 471–482. doi:10.1016/j.epsl.2009.08.33.
- Sohl, F., Spohn, T., 1997. The interior structure of Mars: Implications from SNC meteorites. *J. Geophys. Res.* 106, 23689–23722.
- Solomatov, V.S., Moresi, L.M., 1995. Stagnant lid convection on Venus. *J. Geophys. Res.* 101, 4737–4753.
- Tan, E., Choi, E., Thoutireddy, P., Gurnis, M., Avazis, M., 2006. Geo-framework: Coupling multiple models of mantle convection within a computational framework. *Geochem. Geophys. Geosyst.* 7, Q06001. doi:10.1029/2005GC001155.
- Thomson, B.J., Head, J.W., 2001. Utopia Basin, Mars: Characterization of topography and morphology and assessment of the origin and evolution of basin internal structure. *J. Geophys. Res.* 106, 23209–23230. doi:10.1029/2000JE001355.
- Turcotte, D.L., Schubert, G., 2002. Geodynamics, second ed. Cambridge Univ. Press, Cambridge, UK.
- Wanke, H., Dreibus, G., 1994. Chemistry and accretion history of Mars. *Philos. Trans. R. Soc. A* 349, 285–293.
- Watters, W., Zuber, M.T., Hager, B.H., 2009. Thermal Perturbations caused by large impacts and consequences for mantle convection. *J. Geophys. Res.* 114, E02001.
- Yoder, C.F., Konopliv, A.S., Yuan, D.N., Standish, E.M., Folkner, W.M., 2003. Fluid core size of Mars from detection of the solar tide. *Science* 300, 299–303.
- Zhong, S., Zuber, M.T., Moresi, L., Gurnis, M., 2000. Role of temperature-dependent viscosity and surface plates in spherical shell models of mantle convection. *J. Geophys. Res.* 105, 11063–11082.